Opening and mixed mode fracture processes in a quasi-brittle material via digital imaging

Qing Lin [a,*], Huina Yuan [b], Luigi Biolzi [c], Joseph F. Labuz [d]

[a] College of Petroleum Engineering, China University of Petroleum (Beijing), Beijing 102249, China
[b] State Key Laboratory of Hydroscience and Engineering, Department of Hydraulic Engineering, Tsinghua University, Beijing 100084, China
[c] Department of Structural Engineering, Politecnico di Milano, Milano, Italy
[d] Department of Civil, Environmental, and Geo- Engineering, University of Minnesota, Minneapolis, MN 55455, USA

Article history:
Received 19 September 2013
Received in revised form 23 July 2014
Accepted 25 July 2014
Available online 7 August 2014

1. Introduction

Most experimental studies of fracture in quasi-brittle materials are concerned with mode I deformation, but pure mode I loading seldom represents a realistic condition in the field. *In-situ* situations are often dominated by mixed mode fracture, which displays different characteristics to opening fracture [1,2]. In this paper, the term mixed mode refers to the combination of in-plane modes I and II, without consideration of mode III.

Two fundamental aspects of fracture in a quasi-brittle material are (1) the applicability of linear fracture mechanics, *e.g.* size of the process zone, and (2) the fracture propagation criterion, *e.g.* critical energy release or displacement that governs crack growth. In addition, when a fracture propagates under a non-uniform stress field, self-similarity of fracture will not be maintained and the fracture kinks from the main crack. Under certain conditions, kinking follows a direction of maximum opening displacement, which implies that the mode II stress intensity factor (K_{II}) is zero at the crack tip [3,4]. As a consequence, many attempts to create pure mode II crack growth in the laboratory usually fail [5,6]. Experience has shown that the existence of an opening mode dominates the fracture propagation under mixed mode loading, probably because mode I fracture energy in a quasi-brittle material is much less than mode II fracture energy [7–11].

Furthermore, measurements of displacements along the crack front are rare, and the domination of mode I opening at the crack tip during mixed mode loading has not been directly observed. Rather, experiments that involve an accurate measurement of the structural response (*e.g.* load–deflection) and the trajectory of the crack path, together with fracture propagation

* Corresponding author. Tel.: +86 18210089197.
E-mail address: linx0272@umn.edu (Q. Lin).

Nomenclature

a	notch length
A	transition position
B	specimen thickness
CZ	cohesive zone
h	notch width
H	specimen height
I, I'	intensity value
K_I, K_{II}	stress intensity factor
l	cohesive zone length
M	magnification factor
R	cross correlation function
$\boldsymbol{s}$	separation vector
S	specimen span
SZ	slip zone
Δu	incremental horizontal displacement
Δu_1	incremental normal displacement
Δv	incremental vertical displacement
Δv_1	incremental tangential displacement
w	crack opening displacement
w_c	critical crack opening displacement
θ	inclination angle
β	eccentricity factor
δ	crack sliding displacement

models matching the calculated global response and crack path [4,8,12] predict mode I dominance. Although some works [13,14] have reported crack displacements during mixed mode loading, there were limitations since the experiments were related to fracture initiation and one component of displacement.

Another important aspect is the nonlinear region surrounding the crack tip called the (cohesive) process zone, which can be significant in size for a quasi-brittle material [15,16]. Most studies concerning the cohesive zone are concentrated on pure mode I loading. Some experimental data have indicated that the cohesive zone differs in mode I and mixed mode loading [14,17], but the development of the cohesive zone under mixed mode loading is largely unknown. Characterization of the cohesive zone largely relies on the accurate measurement of displacements near the crack front. However, difficulties arise in estimating the displacements accurately due to the fine resolution of measurements necessary.

Recent advancement of technologies such as high resolution digital cameras and other instrumentation enable the experimental technique known as digital image correlation (DIC) to achieve accurate mapping of full-field displacements. DIC is an optical technique whereby displacements are obtained through comparison of digital images of a specimen surface [18–21]. DIC can be viewed as a modern form of the particle tracking technique, with the tracking target being a "sub-image" having a unique pattern. During an experiment, a charge-coupled device (CCD) or a complementary metal-oxide-semiconductor digital camera is used to acquire a series of digital images. The information, typically full-field displacements, can be extracted by DIC through finding a characteristic pattern within a pair of images. DIC is popular in the study of fracture [22–27] because it has many benefits, such as ease of specimen preparation and simplicity of system setup, as complicated optics are unnecessary.

DIC was used to study the fracture process in a typical quasi-brittle material under the mode I and mixed mode loadings through detailed measurement of displacements surrounding the crack, both at initiation and propagation. The characteristics of the process zone such as length of the zone and critical opening displacement were determined, and the nature of the cohesive process zone was investigated.

2. Experimental technique and setup

2.1. Digital image correlation (DIC)

Modern DIC has its origin from the laser speckle approach. Laser speckles are produced by interference effects through illuminating an optically rough surface with a coherent light. A laser speckle is observed as a spot with a unique size, shape, and intensity value. These unique properties of the speckle are due to the local microscopic surface imperfections on the specimen, such that the speckles move if the specimen undergoes displacement. Thus, these laser speckles can be treated as the signatures on the surface of a specimen and used to evaluate the displacement field [28]. For instance, a numerical analysis based on laser speckles was developed and the concept of small regions, *i.e.* subsets, was introduced [29]. However,

the pattern of the speckles on the images will decorrelate if the displacement to be measured exceeds a certain range or a large out-of-plane displacement occurs. Eventually, artificial speckles called white light speckles (Fig. 1a) that adhere to the surface were used in experiments [18]. A variety of numerical algorithms have been developed through minimizing a correlation coefficient of intensity values of the speckle pattern between two digital images to obtain in-plane displacements [30,31]. A technically similar technique is named particle image velocimetry (PIV), which has been applied to determine deformation of granular materials [19,32]. Regardless of the different names being used, the essential concept of "pattern tracking" is shared for both techniques, only each has its own concentrations because of various purposes and applications.

As a class of noncontacting optical approaches, the concept of DIC is quite intuitive, *i.e.* this group of techniques simply traces a unique feature on the images. Fig. 1a shows two digital images, one with respect to the original surface (reference image) and the other with the deformed surface (current image). A speckle that is circled can be identified in two images. Consequently, based on a global coordinate system, a displacement vector can be determined. However, the irregularity of a speckle makes it inconvenient, if not impossible, for a computer program to identify an individual speckle. A rectangle that contains several speckles with a unique intensity pattern serves as the target and it is named the subset (Fig. 1b). In addition, another relatively small area named the region of interest (ROI) is also selected (Fig. 1b) and it is used as the searching area for a subset. For experiments involving small displacements between two images, an approach based on a fast Fourier transform (FFT) algorithm is advantageous, as the FFT method can reduce computation time in image processing [33,34]. By detecting the peak position of a cross correlation function in the frequency domain, the local displacement vector can be accurately determined in the images.

During DIC processing, there are two digital images, reference and current, recorded with respect to the different loading conditions. A subset containing a unique distribution of intensities is extracted from the two images to determine the

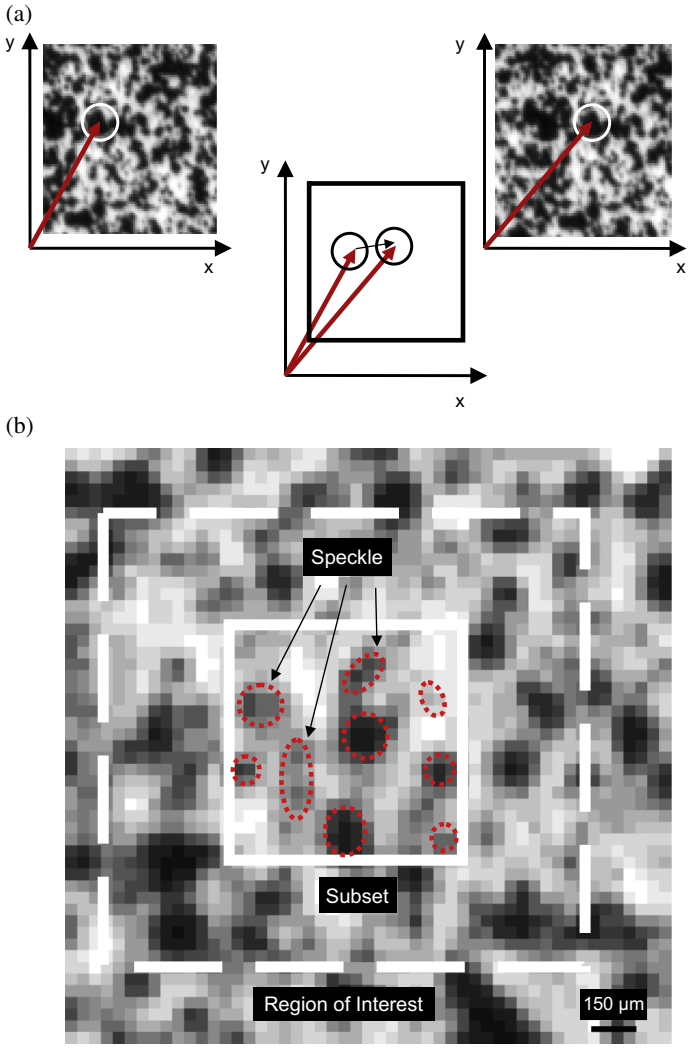

Fig. 1. (a) Speckle motion between two digital images. (b) Digital image, 50 × 50 pixels, with speckles, subset, and region of interest.

displacement vector. The subset and corresponding ROI are first selected in the reference image (Fig. 1b). The intensity values that are located at position P can be represented as

$$I(P) = I(X, Y) \tag{1}$$

It is assumed that the movement of the subset is smaller than the one-half of the ROI size. After displacement u, v, point P moves to position p in the current image. The intensity values are changed to

$$I'(p) = I'(X + u, Y + v) \tag{2}$$

To identify the subset in two images, a cross-correlation method is used to search the intensity values in the ROI. The cross-correlation function $R(\boldsymbol{s})$ is defined as the two-dimensional spatial convolution of I and I' with the separation vector $\boldsymbol{s}$ in the correlation plane:

$$R(\boldsymbol{s}) = \int I(P)I'(p + s)dP \tag{3}$$

A correlation peak is produced in the correlation plane and the position of the peak in the ROI gives the amplitude and direction of the displacement vector. The height of the peak presents the degree of correlation; $R(\boldsymbol{s})$ reaches a maximum in the ROI under the condition $s_x = u$ and $s_y = v$ for a given subset with a unique intensity pattern. The mean displacement of the speckles in the subset, which represents the displacement of the center position of the subset, can be determined. Note that information of displacement inside the subset cannot be obtained, which may pose a problem if the application requires a very high spatial resolution. DIC processing continues with a selection of a new subset, which can be neighbored or overlapped. The complete displacement field is obtained after processing all the subsets in the digital image.

2.2. Experimental setup

The material used for testing, Berea sandstone, consists of uniformly sized grains from 0.1 to 0.8 mm, with the average grain size of 0.2 mm. The properties of the tested sandstone are porosity = 20%, Young's modulus = 10–14 GPa, Poisson's ratio = 0.31–0.34, tensile strength (modulus of rupture) = 3.4–3.6 MPa, and uniaxial compressive strength = 28–32 MPa. All specimens were cut at the same orientation from the same block of rock, which is homogeneous but slightly anisotropic in elastic response.

A simple testing approach to achieve opening or mixed mode fracture is a beam under three-point bending (3 PB) with a center ($\beta = 0\%$) or off-center ($\beta = 20\%, 40\%$) notch, where the eccentricity factor β is the normalized distance, with respect to the half-span, from the centerline (Fig. 2a). Crack initiation and propagation were controlled by a closed-loop, servo-hydraulic system with crack mouth opening displacement (CMOD) as the feedback signal at a rate of 2×10^{-4} mm/s. The nominal size of the beams was height $H = 60$ mm, span $S = 150$ mm, and thickness $B = 25$ mm. Two notch lengths $a = 6$ and 12 mm were used, to give $a/H = 0.1$ and 0.2. Replicate experiments were performed, as shown in Table 1.

A series of twelve specimens were tested, four specimens each for $\beta = 0$, 20, 40%, producing a variety of $K_{II}/K_I = 0$, 4.1, 7.4, 6.1, 11.4%, as determined by a boundary element code [35] assuming linear fracture mechanics applies. The specimen naming, *e.g.* CN-20-1, is associated with "CN" for a center notch, "20" for the notch length being 20% of specimen height, and the second number "1" for the number in the group; specimen EN-20-10-1 means eccentric notch (EN), eccentricity factor β is 20% (20), notch length is 10% of the specimen height (10), and the first specimen in the group (1).

Several considerations need to be satisfied in the experimental setup and specimen preparation to ensure accurate measurements of in-plane displacements. The fundamental importance is the uniqueness of the speckle pattern, especially the pattern within the subset. The prepared speckle pattern has two basic features: the distribution of speckles in the pattern and the average size of the speckles. Well-distributed speckles will help to increase the contrast of the speckle pattern and decrease the measurement bias and noise. Image sampling and selection of subset size fundamentally rely on the average size of the speckles. Fig. 1b shows a typical speckle pattern with 50×50 pixels, where the average size is 5 pixels. Nine speckles, which have various sizes and various intensity values, can be identified randomly inside the subset, as circled in Fig. 1b. A Unibrain (San Ramon, CA) Fire-I 810 IEEE-1394 CCD camera with 1600×1200 effective square pixels was used in combination with a Computer lens (Model M3Z1228MP, Commack NY) with manual control of aperture, focus, and zoom. A typical acquired image from an experiment is shown in Fig. 2b. The software used to perform image correlation was developed by White and Take [32].

A series of calibration experiments were conducted to evaluate the system precision following the procedures used for a speckle interferometry system [36]. Because the matching process was performed on intensity values of the digital images and the "unit" of measure from the computational analysis is pixel-based, an isotropic magnification factor M is introduced to transform the results from the digital image to the physical dimension on the specimen surface:

$$u = Mu^D \text{ and } v = Mv^D \tag{4}$$

where u^D and v^D are the pixel-based displacements from the image analysis. Different magnification factors can be obtained by the adjustment of lens magnification and/or the camera position. However, since the CCD array of the digital camera is fixed (1200×1600), there are limitations in setting M due to the importance of the field of view. Although a smaller magnification factor M produces more accurate experimental measurements, the smaller M also limits the observation region on

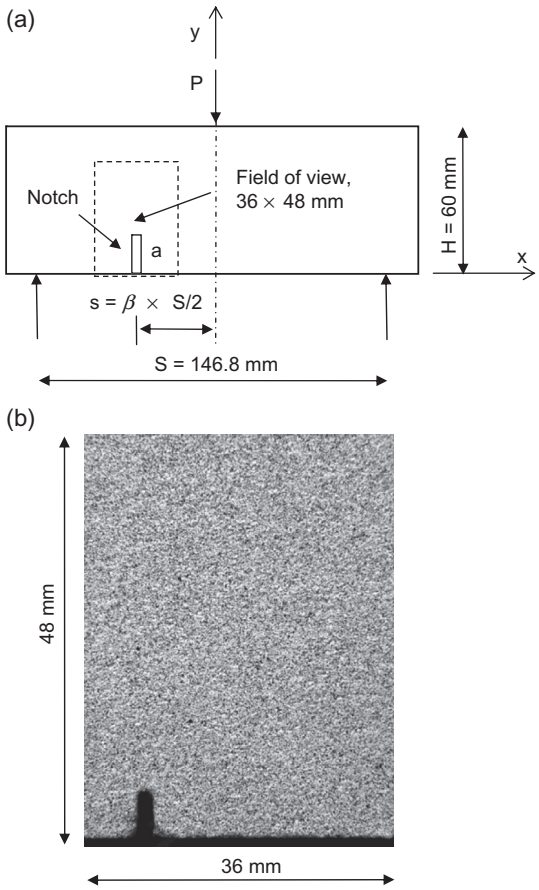

Fig. 2. (a) Loading geometry and observation region on the specimen surface. (b) Typical acquired digital image with an eccentric notch.

Table 1
Specimen dimensions and peak load data.

Test #	CN-10-1	CN-10-2	CN-20-1	CN-20-2	EN-20-10-1	EN-20-10-2	EN-20-20-1	EN-20-20-2	EN-40-10-1	EN-40-10-2	EN-40-20-1	EN-40-20-2
Height H (mm)	62.6	59.6	65.6	59.8	63.8	59.9	62.4	62.6	60.8	62.8	59.7	59.4
Thickness B (mm)	26.7	25.3	29.3	25.6	27.1	24.4	24.3	23.6	25.1	24.8	25.4	26.1
Span S (mm)	146.8	146.8	146.8	146.8	146.8	146.8	146.8	146.8	146.8	146.8	146.8	146.8
Notch length a (mm)	5.3	6.0	13.4	10.9	5.3	6.4	12.0	11.6	6.4	6.6	12.1	12.0
Notch width h (mm)	1.2	N/A	1.4	1.2	1.8	1.2	1.5	1.1	1.1	1.4	1.4	1.4
Eccentricity factor β	0	0	0	0	4.1%	4.1%	7.4%	7.4%	6.1%	6.1%	11.4%	11.4%
Peak load (N)	1170	959	1034	784	1456	892	738	743	1317	1245	880	933
Opening displacement at peak (μm)	30	27	35	26	48	44	46	40	38	40	52	44
Opening zone length at peak (mm)	7	7	6	6	10	10	12	10	12	10	12	11

the specimen surface. Eventually, a magnification factor $M = 30$ μm/pixel was selected with the observation area of 36×48 mm, because the height of the specimen was around 60 mm (Fig. 2b). In summary, the features of the DIC system are subset size of 20 pixels, magnification factor $M = 30$ μm/pixel, system precision of 0.3 μm, and measurement grid of 80×60 points.

3. Opening mode fracture tests

To demonstrate the utility of DIC in characterizing the fracture process, a mode I fracture test is described; further details are presented in [27]. Typical loading curves including load *vs* CMOD and load *vs* load-point displacement (deflection) are shown in Fig. 3. Generally, a small seating load, 10–15% of the peak load, was applied to the specimen before starting the

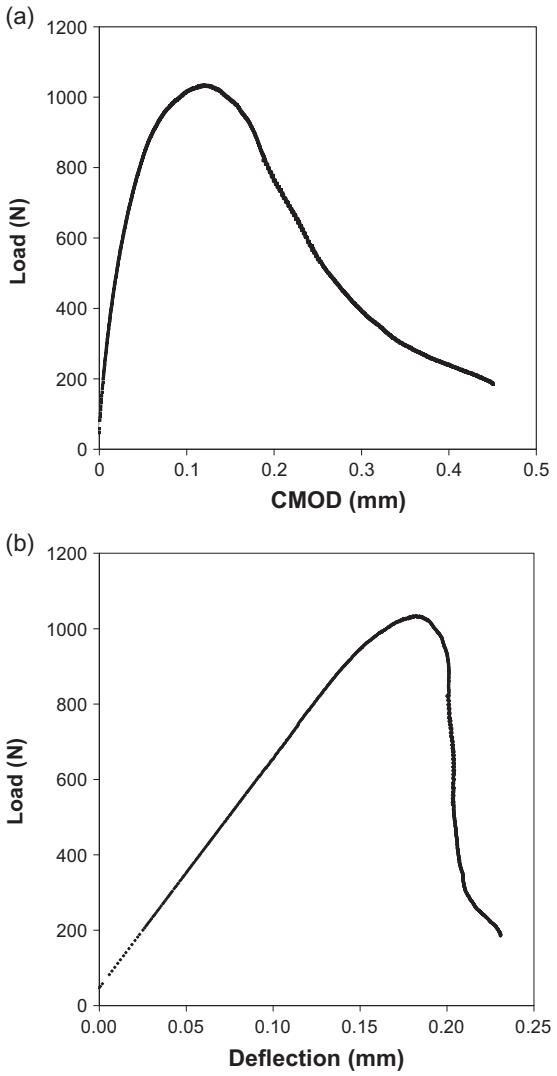

Fig. 3. Loading history, specimen CN-20-1. (a) Crack mouth opening displacement (CMOD); (b) load-point deflection.

experiment. Based on CMOD as the feedback signal, the crack initiated and propagated in a controlled manner, even though the energy stored in the specimen is sufficient to propagate the crack without additional external energy (Fig. 3b). Displacement contours associated with various loading stages from pre-peak to post-peak are constructed. The measured displacements are based on the comparison of two digital images; thus they are *incremental* displacements between two conditions.

Fig. 4 shows the displacement contours of specimen CN-20-1 with respect to different loading stages. Fig. 4a and b indicate the elastic deformation of the specimen (40–60% peak). The horizontal displacement contour exhibits a symmetric pattern surrounding the notch. Clearly the neutral axis is at the cross section $y = 45$ mm. The vertical cross section at $x = 0$ mm can be treated as the line of symmetry (Fig. 4a), where the horizontal displacement $u = 0$, due to the 3 PB loading configuration. Similar to the fringe pattern obtained from speckle pattern interferometry [14], the iso-displacement lines were drawn in the contour to help interpret the pattern: the lines merge at the notch tip and they are distributed symmetrically along the line of symmetry. The vertical displacement contour displays a displacement pattern that agrees with the "stubby" 3 PB beam with some effect at the position of the applied load, such that the vertical displacement decreases along the center cross section. Because of the limited observation region, the load position cannot be observed, but the vertical displacement is still found to reduce from -19 μm to -14 μm, where the negative sign means the displacement is opposite to the positive direction of the y-axis, and the specimen moves down. When moving away from the loading position, the influence of the load point decreases and the vertical displacements are more or less the same. Of course, the existence of the notch has a consequence of slightly more vertical displacements surrounding it (Fig. 4b).

As the applied load increased, a displacement discontinuity formed, as shown in Fig. 4c (80–90% peak). Similarly, the iso-displacement lines demonstrated that the merged position is at $x = 0$ mm, $y = 15$ mm, such that a "fracture" initiated. The

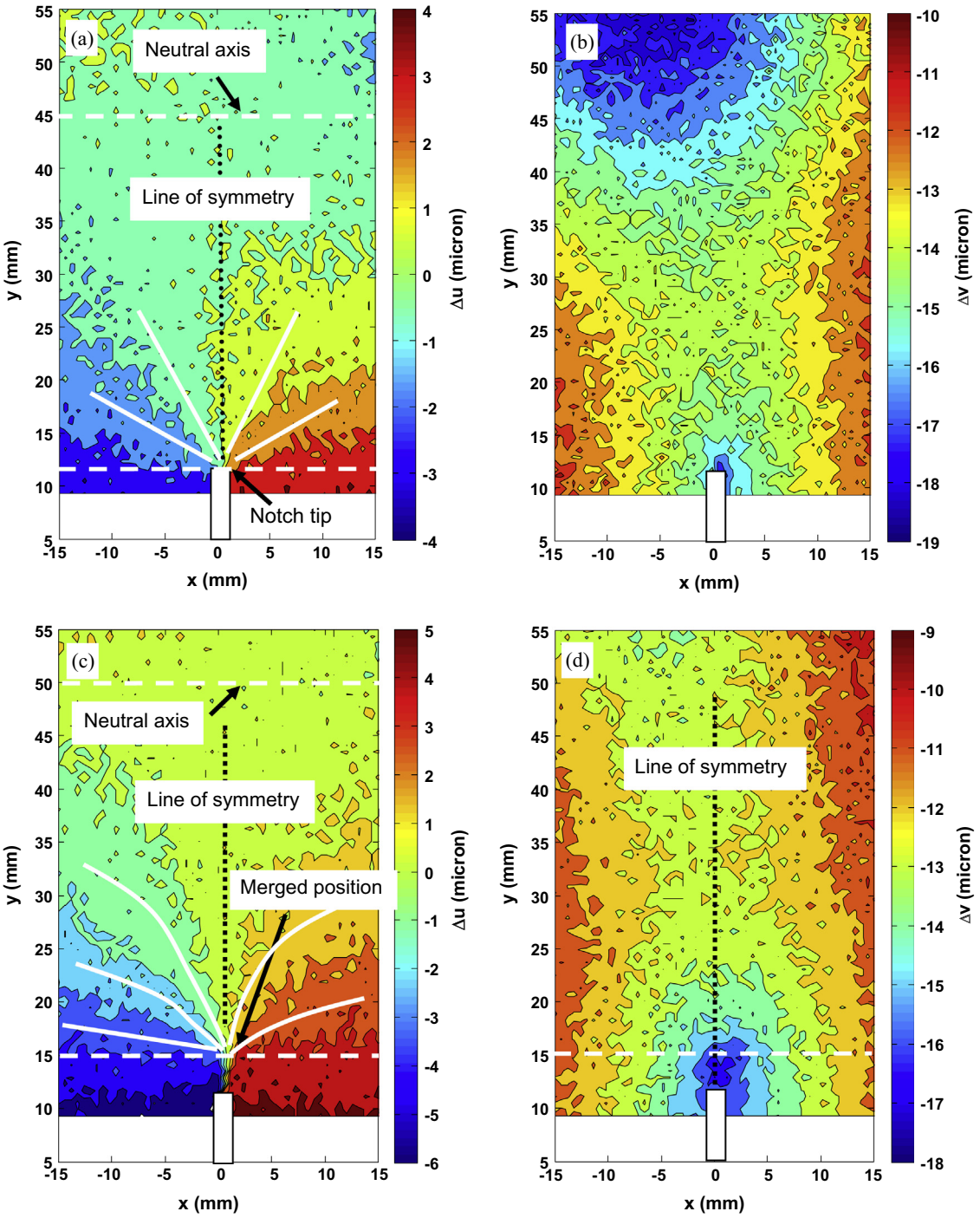

Fig. 4. Incremental horizontal and vertical displacement contours, specimen CN-20-1, where CZ = cohesive zone; (a) and (b) 40–60% peak; (c) and (d) 80–90% peak; (e) and (f) 98–100% peak, (g) and (h) 95–90% post-peak; (i) and (j) 80–70% post-peak.

neutral axis also moved to the cross section $y = 50$ mm. The incremental horizontal displacement pattern at the upper area of the merged position is similar to the pattern above the notch in Fig. 4a. However, the displacements are observed to have a "jump" below it, *e.g.* the change from −5 μm to +5 μm at two sides of the symmetry line ($x = 0$ mm) close to the tip of notch. Of course, the opening displacement is zero at the tip. As shown in Fig. 4c, the merged point separates the symmetry line into two sections: the opening displacement is zero above the point and below it the displacement is larger than zero. The

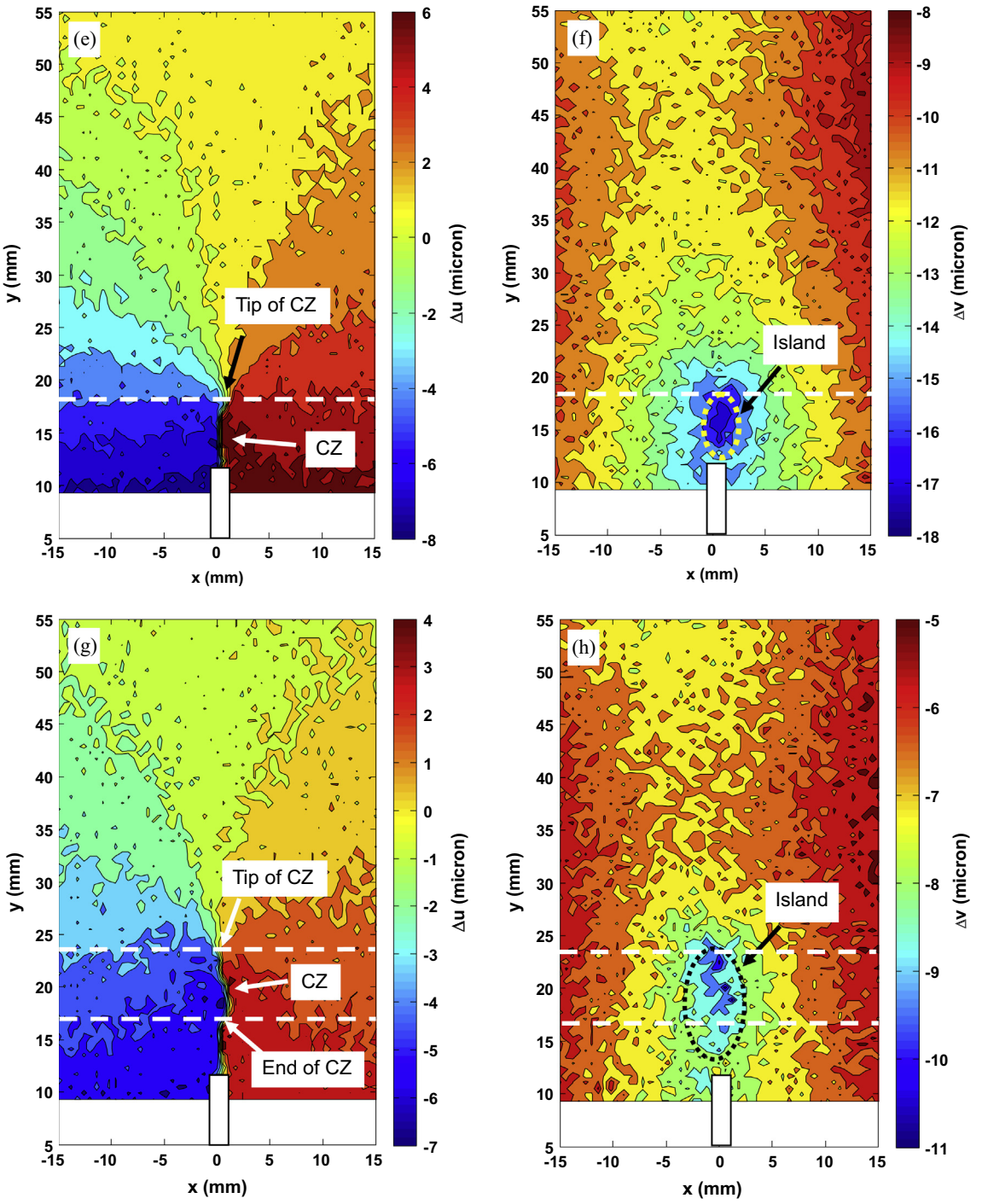

Fig. 4 (*continued*)

opening displacement can be interpreted as the existence of a cohesive zone. Because the applied load did not reach the peak, it is reasonable to assume that the displacement discontinuity still can transfer stress. Thus, the displacement discontinuity is the cohesive zone and the merged position is the tip.

The incremental vertical displacement Δv contours cannot detect the effect of the point load, as it was out of the observation area (Fig. 4d). However, more Δv is observed to concentrate surrounding the notch, especially a small region of larger incremental vertical displacement $\Delta v = -17$ μm above the notch tip. As shown in Fig. 4d, it was below the intersection between the symmetry line and cross section $y = 15$ mm, the position of the tip. Thus, this region coincided with the cohesive

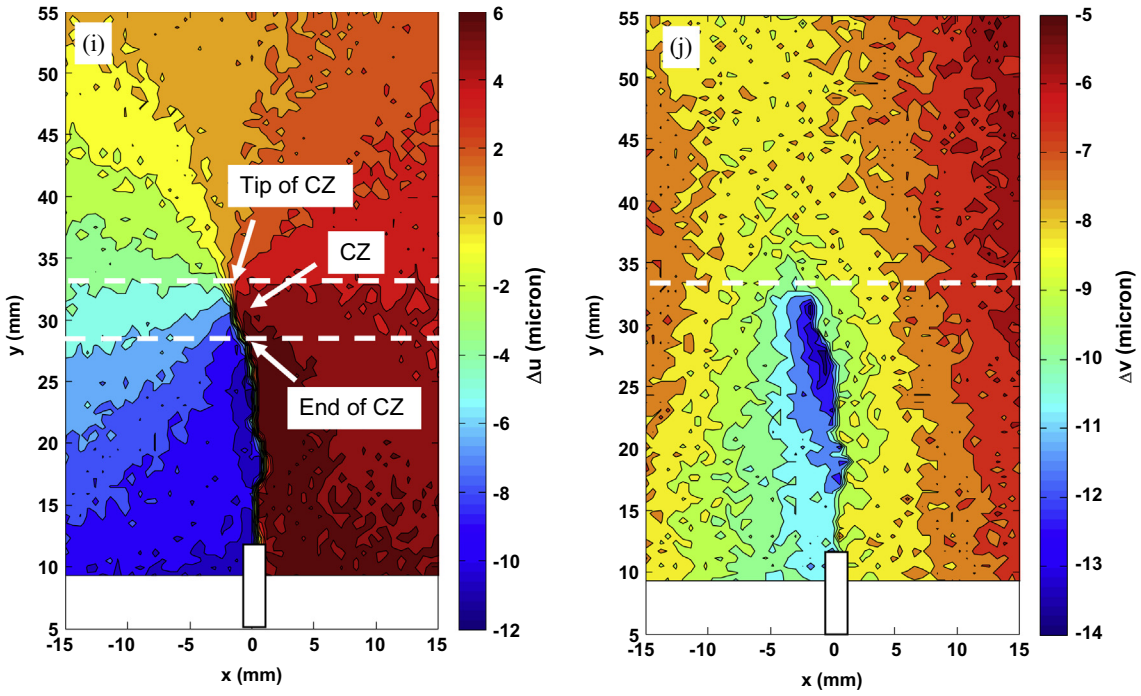

Fig. 4 (*continued*)

zone identified from horizontal displacements. Since the cohesive zone implies localized damage, it is reasonable that more vertical displacement may occur inside the zone.

When the peak load was reached (98–100% peak), the merged point moved to the position $y = 18$ mm. The section between it and the notch tip is the cohesive zone, about 6 mm in length (Fig. 4e). With the small increasing load (98–100% peak), the incremental horizontal displacement jumps from −8 μm to +6 μm at the two sides of the notch tip. The incremental vertical displacement contours (Fig. 4f) show the region of larger displacement above the notch also extended. An "island" with Δv larger than 16 μm, as circled in Fig. 4f, occupied the area of the cohesive zone. The width can be estimated as 5 mm, based on vertical displacement contours.

After the applied load passed peak, the fracture propagated and the vertical displacement islands also moved upwards. Fig. 4g and h show the displacement contours associated with the post-peak loading (95–90%). The tip of the cohesive zone is identified at $y = 24$ mm (Fig. 4g) from the horizontal displacement contours. An island of incremental vertical displacement $\Delta v = -9$ μm, as circled in Fig. 4h, covers the region between $y = 14$ and 25 mm. With increasing CMOD (load decreasing), the fracture path became tortuous, possibly due to material heterogeneity or loading imperfections. For instance, when the load decreased from 80% to 70% of peak, the tortuosity of fracture is clearly indicated in Fig. 4i; the tip is at $y = 33$ mm and almost twice the horizontal displacement is observed on the left side than the right (12 and 6 μm); the Δv contours also gives an identical picture of the crack path (Fig. 4j). A fundamental difference in vertical displacements between Fig. 4j and earlier loadings is due to crack tortuosity, such that the islands of larger vertical displacements are switched to the left and they are not symmetric along the cross section $x = 0$ mm.

The detailed analyses of the displacement contours provide the opening displacement profiles along the cohesive zone, as shown in Fig. 5. Because the DIC algorithm involves larger computation errors if the displacement gradient is large, the displacements are evaluated a short distance from the symmetry line at $x = \pm 2$ mm and not directly on the crack face. Although the measurements involved incremental displacements, the total displacements can be obtained through a summation from initiation to post-peak condition (Fig. 5). Actually, there is a small opening displacement, 1–3 μm, at the tip of the cohesive zone, simply because the displacements cannot be evaluated on the crack face ($x = 0$ mm).

The maximum crack opening displacement at peak load is regarded as the critical value ω_c that separates the cohesive zone from a traction-free crack, and the cohesive zone is assumed to be fully developed at peak load as the crack propagates in an unstable manner. The loading geometry and specimen size may also influence the development of the cohesive zone [37,38], and certainly the specimen height must be larger than the length of the cohesive zone. Nevertheless, the critical crack opening displacement at peak load represents a reference value for the material, regardless of testing configuration. By taking it as the critical value, the cohesive zone can be tracked.

Fig. 5 shows the crack opening displacement profiles of specimen CN-20-1 with respect to the various loading stages. The critical crack opening displacement was $\omega_c = 35$ μm at peak and the corresponding length of the zone was 6 mm (Fig. 4e).

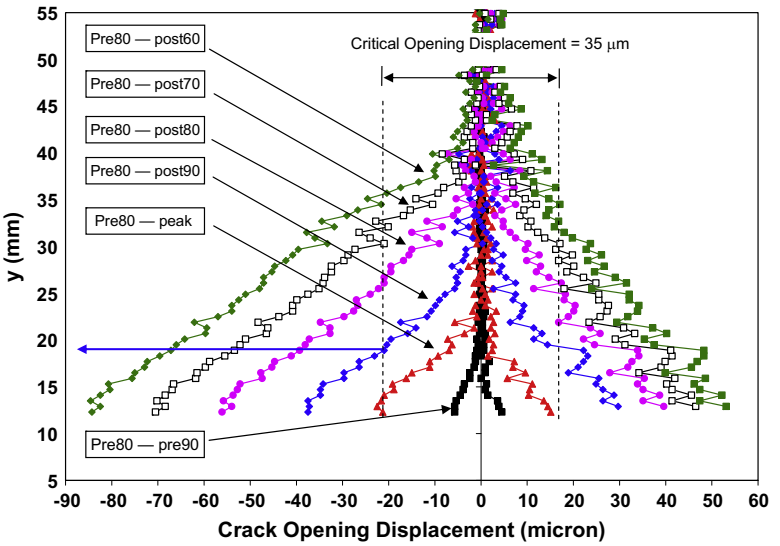

Fig. 5. Total opening displacement along the fracture, specimen CN-20-1.

Based on ω_c = 35 μm, the end of cohesive zone related to various loadings (crack lengths) can be identified from the displacement profile. For example, the end of the zone was observed at y = 19 mm for post-peak loading of 90% in Fig. 5; since the tip of the zone was at y = 24 mm, the zone length was 5 mm, as shown in Fig. 4g. Note that the fracture tortuosity may influence the measurement of the cohesive zone, *e.g.* a shorter zone (4 mm) was determined in Fig. 4i because the end of zone was at y = 29 mm in the displacement profile.

The other center notch specimens with different notch length exhibit a similar value of the critical opening displacement ω_c and zone length l at peak, as shown in Table 1. The average value of ω_c = 30 μm is considered a material property for the Berea sandstone, which agrees well with the measurements from speckle pattern interferometry [14].

4. Mixed mode fracture tests

Specimens with various eccentric notch positions under three-point bending were used to produce mixed mode fracture; the testing configuration and the observation region are shown in Fig. 2. Similar to opening mode fracture, the construction of displacement contours were from the pre-peak to post-peak loading. In all tests, the crack initiates and eventually propagates from the notch tip and the crack trajectory is angled towards the applied load at the centerline.

4.1. Eccentric notch specimens – 20% position

Fig. 6 shows the displacement contours from specimen EN-20-10-1, and the contours are considered to be associated with elastic deformation since they are in the early loading stage (30–60% peak). Clearly, the neutral axis can be identified from the horizontal displacement. It is observed that the existence of the notch does not change the displacement pattern fundamentally; the contours are similar to pure mode I displacements. However, the displacements surrounding the notch are quite different; *e.g.* the "zero" horizontal displacement is distorted to the right side of the notch. Furthermore, more horizontal displacements are recognized on the left side of notch than the right: Fig. 6 indicates that the horizontal displacement is −10 μm on the left compared to +2 μm on the right side of the notch, a consequence of mode II deformation. The twisted vertical displacement contour also exhibits the influence of mode II loading.

A zone of displacement discontinuity started to develop near the notch tip when the load increased to 70% of peak, and the zone extended as the load increased. Fig. 7a and b display the incremental horizontal and vertical displacements Δu, Δv from specimen EN-20-10-1 at the load of 98–100% peak. Both horizontal and vertical displacements are twisted due to the mixed mode loading; *e.g.* there is more horizontal displacement on the left side of the zone and more vertical displacement is present on the right side. Even though the displacements are distorted, a merged position where the horizontal displacements merge can still be recognized at x = −10 mm, y = 14 mm. As shown in Fig. 7a, this displacement discontinuity zone can be clearly observed under the merged point and this zone is inclined at θ = 18° from vertical. However, it is difficult to observe any location related to this zone from the vertical displacements (Fig. 7b), in contrast to the mode I experiments. It is essential to obtain the normal and tangential displacements along the zone, since they are of interest for investigating the fracture process, rather than the horizontal and vertical displacements.

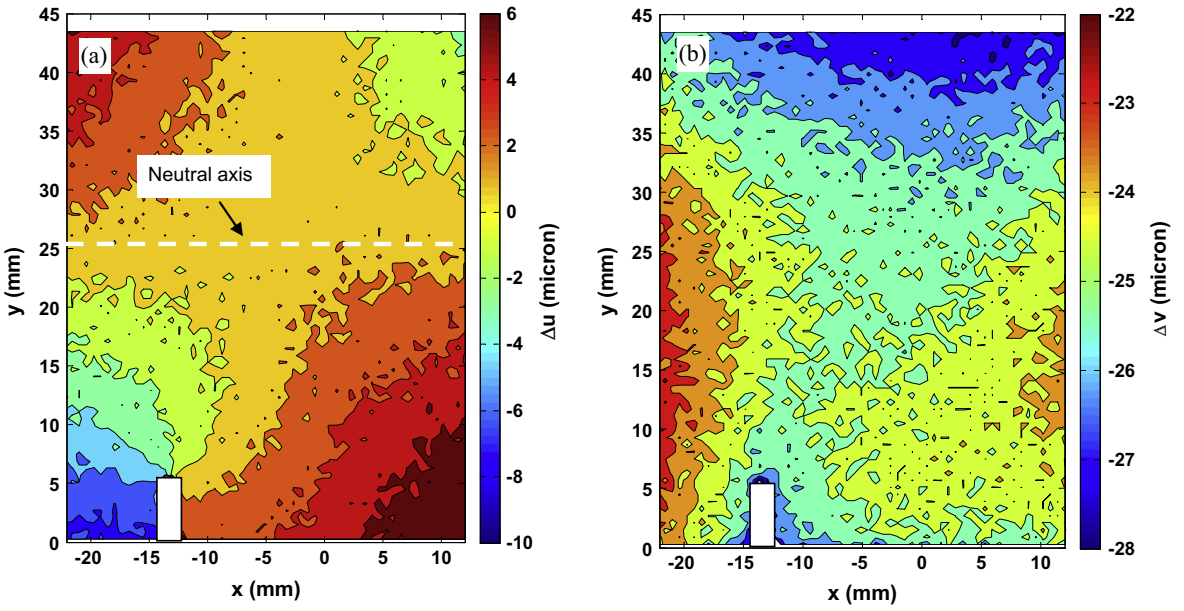

Fig. 6. Displacement contours, specimen EN-20-10-1, 30–60% peak. (a) Incremental horizontal displacement Δu; (b) incremental vertical displacement Δv.

Thus, a new coordinate system (x_1, y_1) is established at the notch tip and the axis y_1 is along the direction of the fracture, inclined at 18° from vertical, as shown in Fig. 7c and d. Even with a slight tortuoisty of the fracture, basically crack growth was planar. Since the information of full-field displacements $(\Delta u, \Delta v)$ is available, the displacements $(\Delta u_1, \Delta v_1)$ based on the new coordinate system can be computed through a transformation of the horizontal and vertical displacements. Fig. 7c and d displays the transformed displacements Δu_1, Δv_1 in the coordinate system (x, y).

The displacements Δu_1, Δv_1 are the incremental normal and tangential displacements along the zone of displacement discontinuity, the eventual fracture. Similarly, the iso-displacement lines can be drawn in the normal (opening) displacement contour, and they identify the tip at the position $x = -10$ mm, $y = 14$ mm (also identified from the horizontal displacements). Similar to the mode I specimen (Fig. 4a), the merged position has a fundamental role, such that the normal displacements above the location are zero along the axis y_1, but they switch to nonzero values below it (Fig. 7c). Again, it is assumed that the critical displacement is reached at peak load. Since the notch tip is at the position, $x = -13$ mm, $y = 6$ mm, the length of the cohesive (opening) zone is about 10 mm after the transformation to the y_1 axis.

More interesting are the tangential displacement contours, as an island that is circled in Fig. 7d occupied the area of the cohesive zone. It shows that there are no differences, or very little difference, between the tangential displacements from the two sides of the cohesive zone, indicating an absence of mode II deformation. Although the tangential displacements outside the influence of the cohesive zone display a different pattern, the tangential displacements in the region surrounding the cohesive zone show no differential movement, and the tangential displacements can be regarded as a symmetric pattern. Thus, it can be concluded that fracture initiation under mixed mode loading for the 20% position is due to mode I deformation, as opening prevails near the crack tip.

Under CMOD control, crack growth can be followed as the applied load decreases in the post-peak region. The incremental normal and tangential displacements Δu_1, Δv_1, as shown in Fig. 8, provide a clear picture about mixed mode crack propagation. Here, it is important to emphasize two points: (1) two coordinate systems (x, y) and (x_1, y_1) are used together to present the experimental results. The displacements Δu_1, Δv_1, are based on (x_1, y_1) because they represent the normal and tangential displacements. However, they are plotted in (x, y) because it is convenient for the comparison with the opening mode fracture. Thus, the following figures plot the normal and tangential displacements Δu_1, Δv_1, in x, y. (2) Because the two coordinates systems (x, y) and (x_1, y_1) are linearly transformed, the displacement gradients are also linearly related. For example, $\frac{\partial \Delta u_1}{\partial y_1}$ and $\frac{\partial \Delta v_1}{\partial y_1}$ are linearly related to the gradients $\frac{\partial \Delta u_1}{\partial y}$ and $\frac{\partial \Delta v_1}{\partial y}$. It implies that the observations between $\frac{\partial \Delta u_1}{\partial y}$ and $\frac{\partial \Delta u_1}{\partial y_1}$ are similar. Thus, the characteristics of displacement profiles Δu_1, Δv_1, remain the same, regardless of the coordinate system.

In Fig. 8a, according to the normal displacement contours, the position A_1, $x = -7$ mm, $y = 29$ mm is identified as the tip of the cohesive zone, where the iso-displacement lines are merged. Similar to opening mode specimens, it is necessary to evaluate the crack opening and sliding displacements. Thus, two cross-sections that are close to the cohesive zone y_1-axis, ±2 mm, are selected to represent its two "sides" because of the relatively coarse DIC computation positions (0.6 mm). The normal and tangential displacements along the two sides are plotted in Fig. 8b and d. Note that the displacements are selected from the y_1 axis, but it is plotted in the y-axis. Fig. 8b displays the distribution of opening displacements along the cohesive zone, which is similar to the opening mode specimen, only more displacements are observed in the left side probably due to the tortuous nature of the crack from the mixed mode deformation.

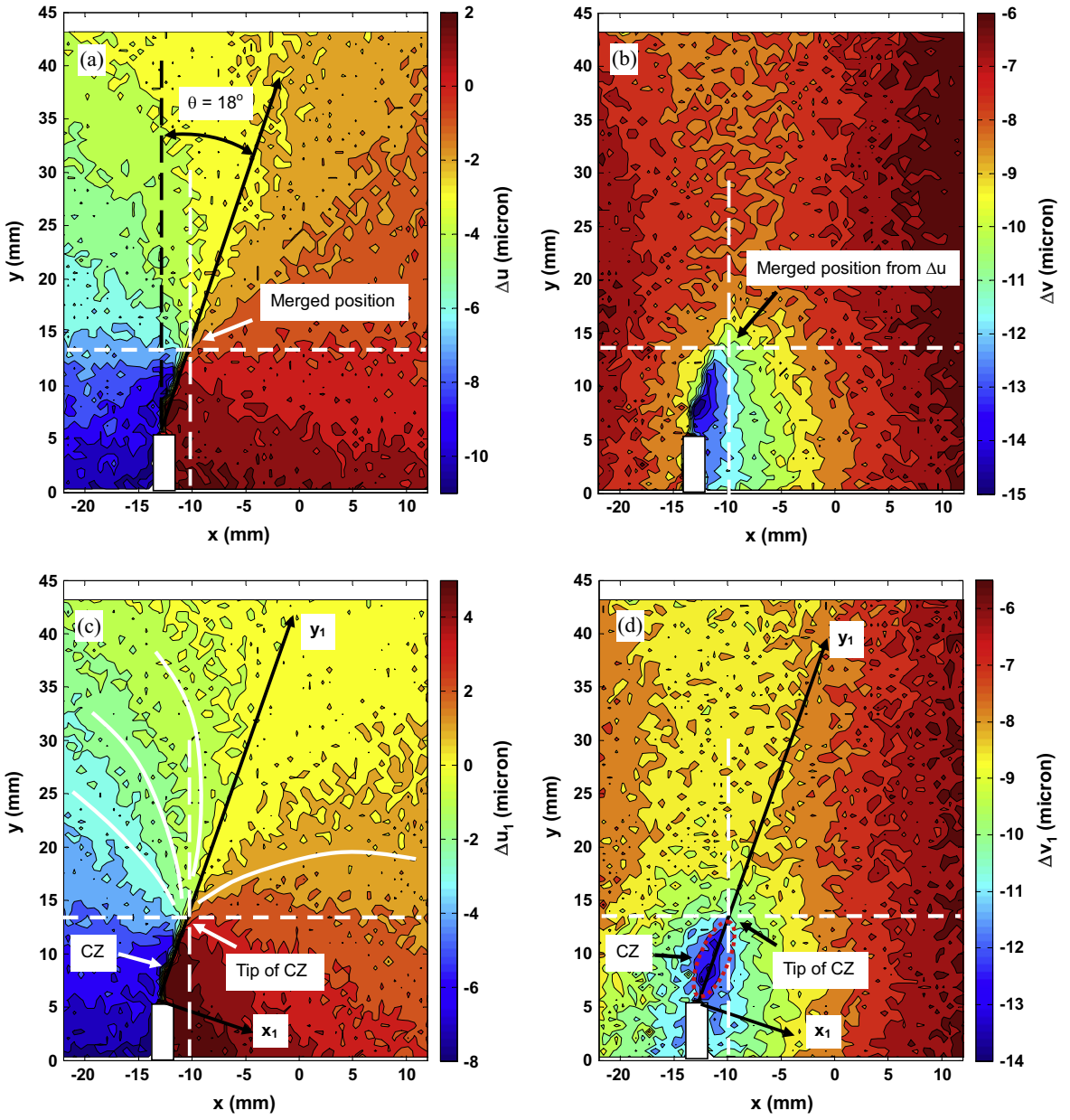

Fig. 7. Displacement contours of specimen EN-20-10-1, 98–100% peak, where CZ = cohesive zone; (a) Incremental horizontal displacement Δu; (b) incremental vertical displacement Δv; (c) incremental normal displacement Δu_1; (d) incremental tangential displacement Δv_1.

The incremental tangential displacements indicate the influence of shearing stresses, and the tangential displacements differences, *i.e.* the sliding displacements along two sides of the cohesive zone implies the existence of mode II deformation (Fig. 8c). An interesting phenomenon is observed at a transition position A_2, $x = -10$ mm, $y = 18$ mm, from tangential displacements. Above the position, the difference of the tangential displacements along the cohesive zone is small, as circled in Fig. 8c and implies that it is an opening zone without sliding. However, the tangential displacements exhibit a displacement "jump" below it. Through the inspection of the tangential displacement profiles along the cohesive zone (Fig. 8d), the two profiles initially are very close and then start to split at position A_2. This position divides the cohesive zone into two parts, one has no (or very little) sliding displacement, and the other can be observed to have sliding displacement. Hence, the zone below position A_2 is a slip zone (SZ), and A_2 is the beginning location of the slip zone or the end of the cohesive zone for mixed mode specimens. The determination of the end position of the cohesive zone after the peak, similar to mode I specimens, is based on the critical opening displacement.

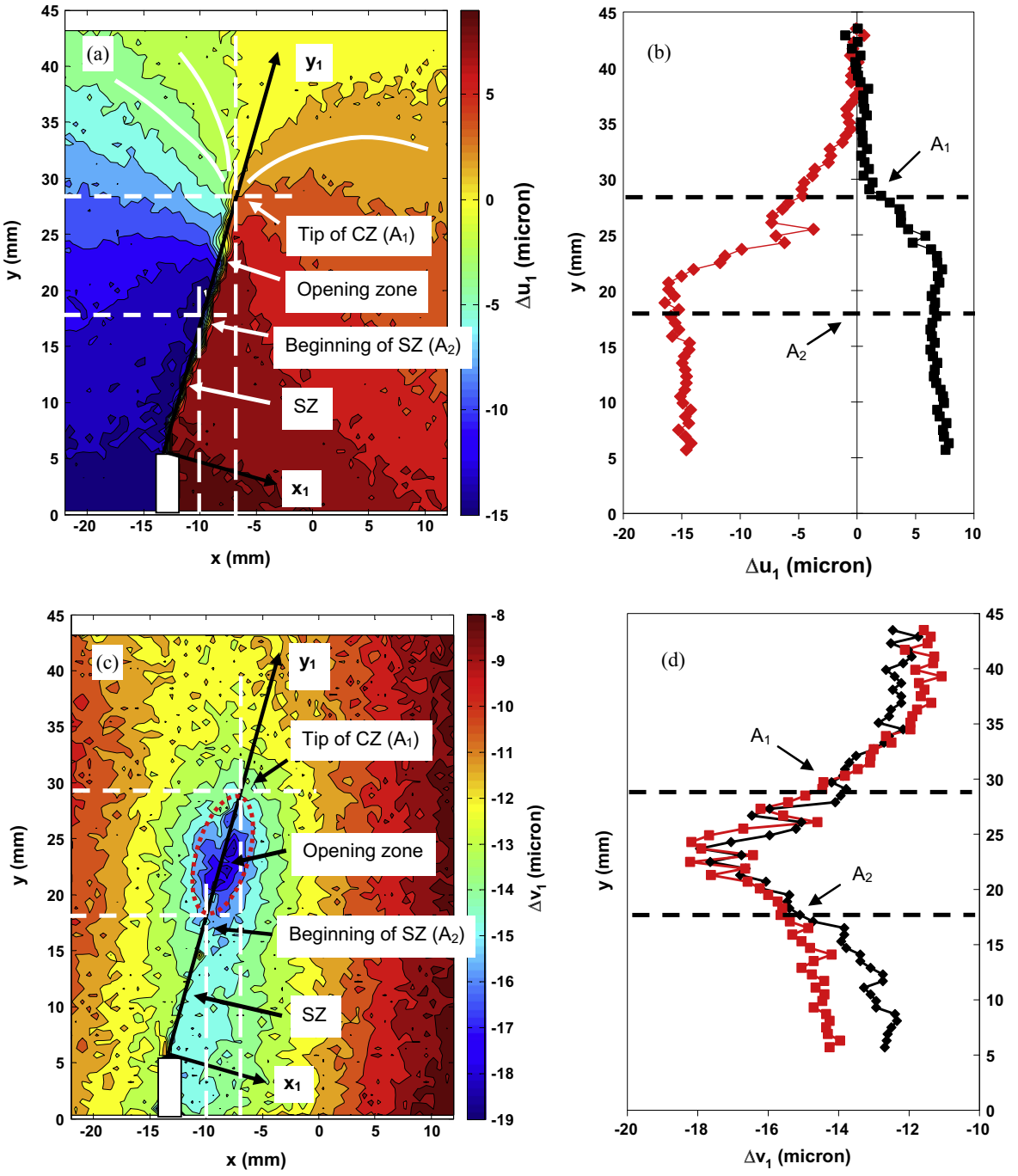

Fig. 8. Incremental displacements of specimen, EN-20-10-1, 80–70% post-peak, where SZ = slip zone. (a) Contours of incremental normal displacement Δu_1; (b) profile of Δu_1 along the fracture; (c) contours of incremental tangential displacement Δv_1; (d) profile of Δv_1 along the fracture.

It is worth emphasizing that a large gradient of incremental displacement $\frac{\partial \Delta u_1}{\partial y}$ is observed in the cohesive zone between positions A_1 and A_2, and it is almost zero outside the zone (Fig. 8b). This opening displacement gradient is much larger (20–30 times) inside the zone, and its sudden change when it is outside may be due to the absence of cohesive traction. Modeling is needed to validate this hypothesis.

Combining the information from the normal and tangential displacements, two regions can be clearly identified, an opening zone with no sliding, and a zone with opening and sliding together, as shown in Fig. 8. From the tip of the cohesive zone A_1 to the location A_2, it is only opening, the length of which is about 12 mm; the rest of the zone is a region with opening and

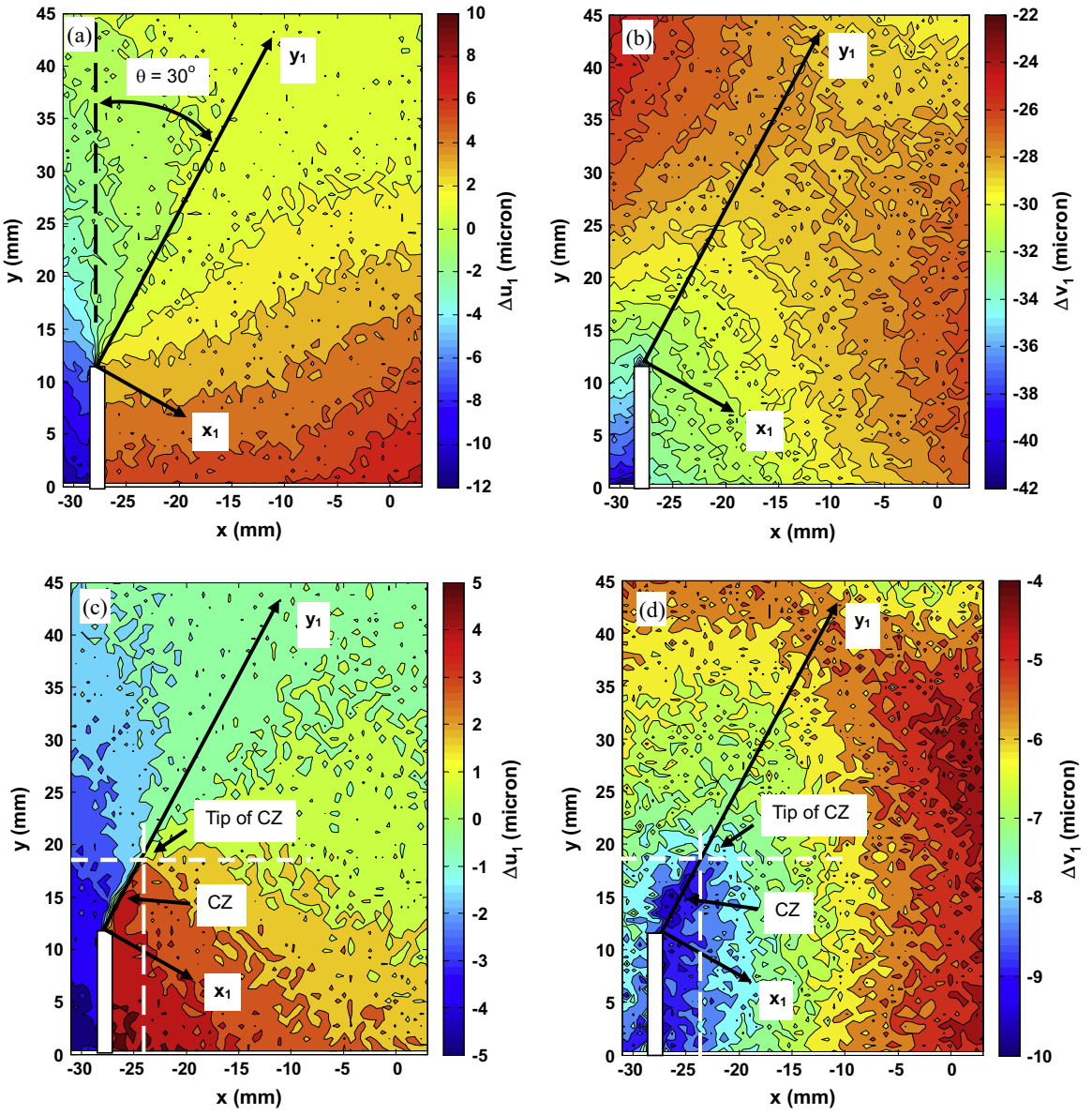

Fig. 9. Incremental normal and tangential displacement contours, specimen EN-40-20-2. (a) and (b) 60–80% peak; (c) and (d) 98–100% peak; (e) and (f) 95–90% post-peak; (g) and (h) 80–70% post-peak; (i) and (j) 70–60% post-peak.

sliding. Thus, mode II displacement does not exist near the tip and mode I dominates in mixed mode fracture propagation for the $\beta = 20\%$ notch position ($K_{II}/K_I = 4.1\%$).

4.2. Eccentric Notch Specimens – 40% position

With a deeper notch further from the center, a larger value of $K_{II}/K_I = 11.4\%$ is created at the notch tip, representing a greater influence of mode II loading. Fig. 9 shows a sequence of incremental displacement contours from specimen EN-40-20-2. Since the fracture kinked from the notch tip, inclined at $\theta = 30°$ from vertical, a new coordinate system (x_1, y_1) is setup and the incremental normal and tangential displacements Δu_1, Δv_1 are obtained. Fig. 9a and b show the displacements with respect to early loading (60–80% peak), normal (opening) displacements display a symmetric pattern along the y_1-axis and zero displacement can also be identified. The tangential displacements indicate some effect due to the load at the center of the beam, and the existence of the notch also influences the displacement pattern since more displacements are observed above the notch tip. The fracture initiated in the specimen as the applied load increased to peak. As shown in Fig. 9c and d (98–100% peak), a cohesive zone was developed and the tip is identified at $x = -24$ mm, $y = 19$ mm. The incremental

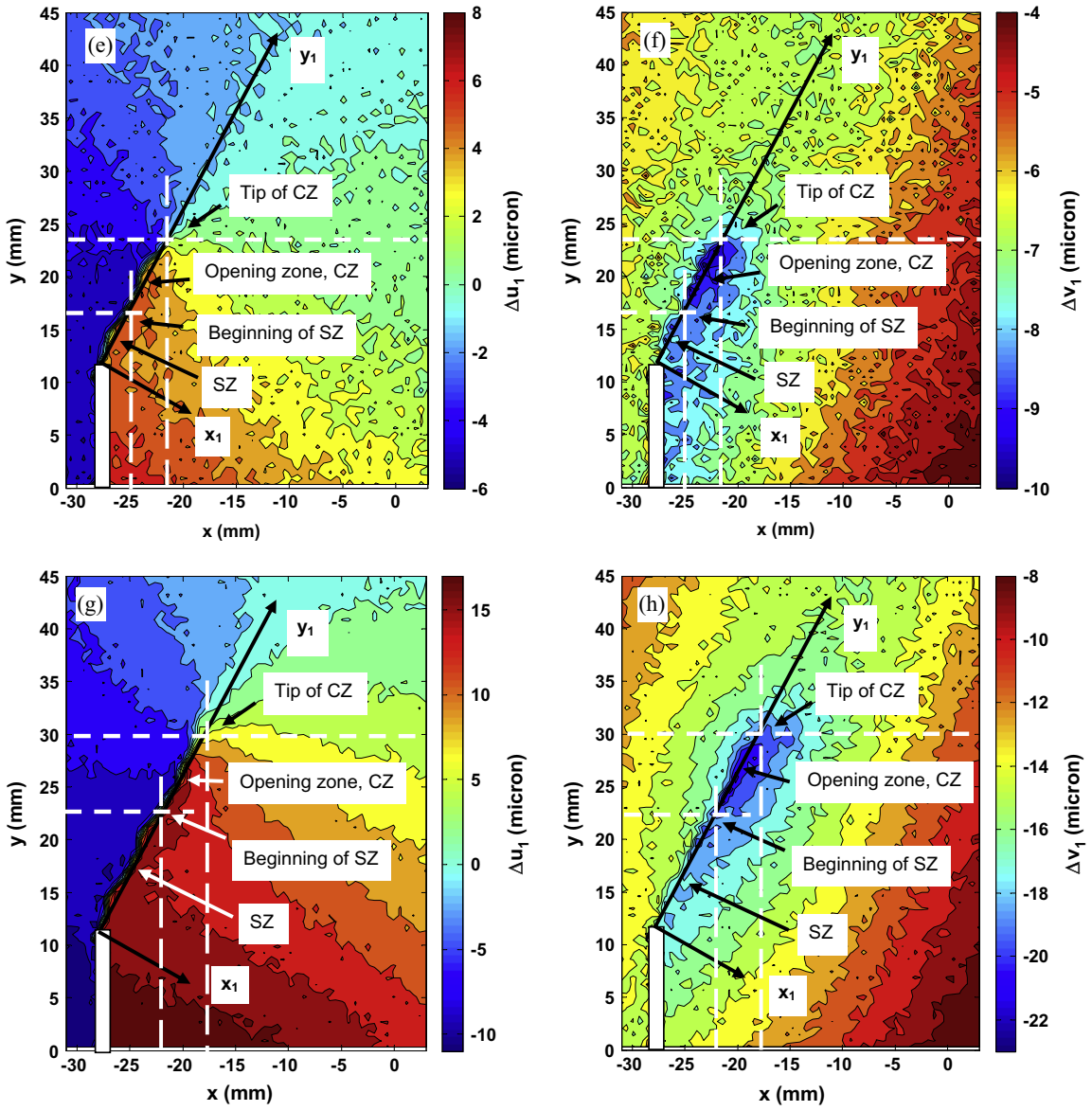

Fig. 9 (*continued*)

tangential displacement islands are observed around the notch tip and they developed symmetrically along the y_1-axis, which implies that it is an opening zone. Again, no occurrence of sliding (mode II displacement) was observed. The cohesive zone at peak was 11 mm long, almost twice that of specimen CN-20-1 (Fig. 4e).

As the crack propagated and load decreased to 90% of peak, the tip of the cohesive zone was observed at the position $x = -22$ mm, $y = 24$ mm (Fig. 9e). A slip zone starts to appear in the specimen, as shown in Fig. 9f, and it starts at $x = -25$ mm, $y = 16$ mm. The length of the opening zone was determined to be 10 mm. As the fracture propagated deeper into the specimen, the opening zone was 10 mm and 11 mm long for two different loadings, 80–70% (Fig. 9g and h) and 70–60% (Fig. 9i and j) of peak respectively. The length of the opening zone was observed to be approximately constant under mixed mode propagation for the loading conditions investigated.

The crack opening and sliding displacements can be determined through the summation of incremental displacements, as shown in Fig. 10. Fig. 10a displays the opening displacements with respect to a variety of loading stages along the y-axis. At peak, the maximum crack opening is assumed to be the critical crack opening displacement, $\omega_c = 44$ μm. The experimental results from the other specimens (Table 1) also indicate that the critical crack opening displacements at peak are about 50% larger than the mode I tests. Fig. 10b gives the information about the crack sliding displacements δ at the various loadings. The sliding displacements cannot be identified in the displacement contours until the post-peak load passed 95% peak. Note

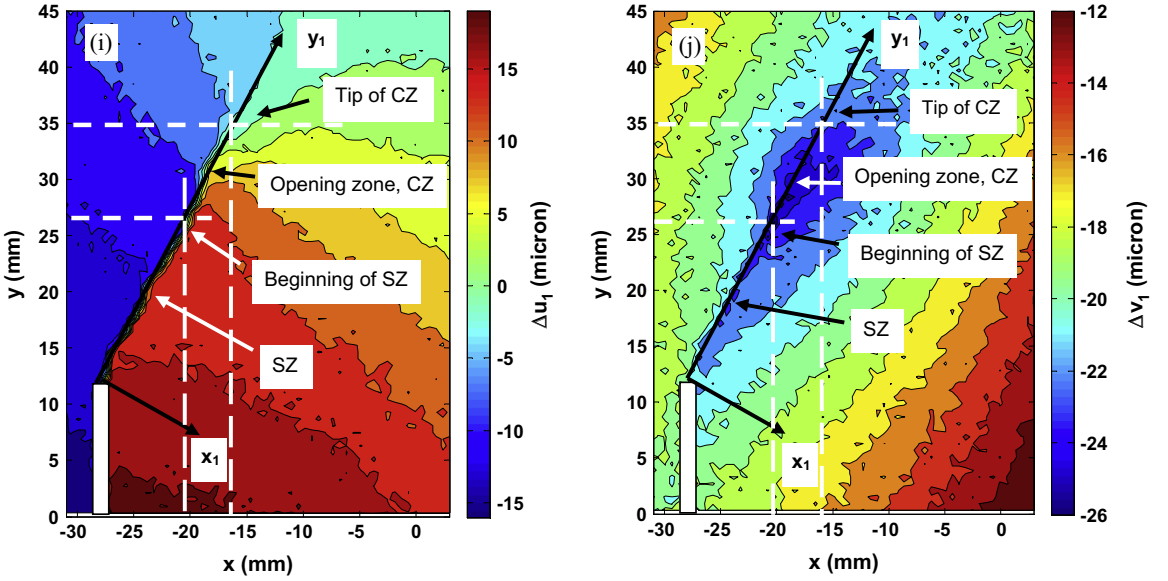

Fig. 9 (*continued*)

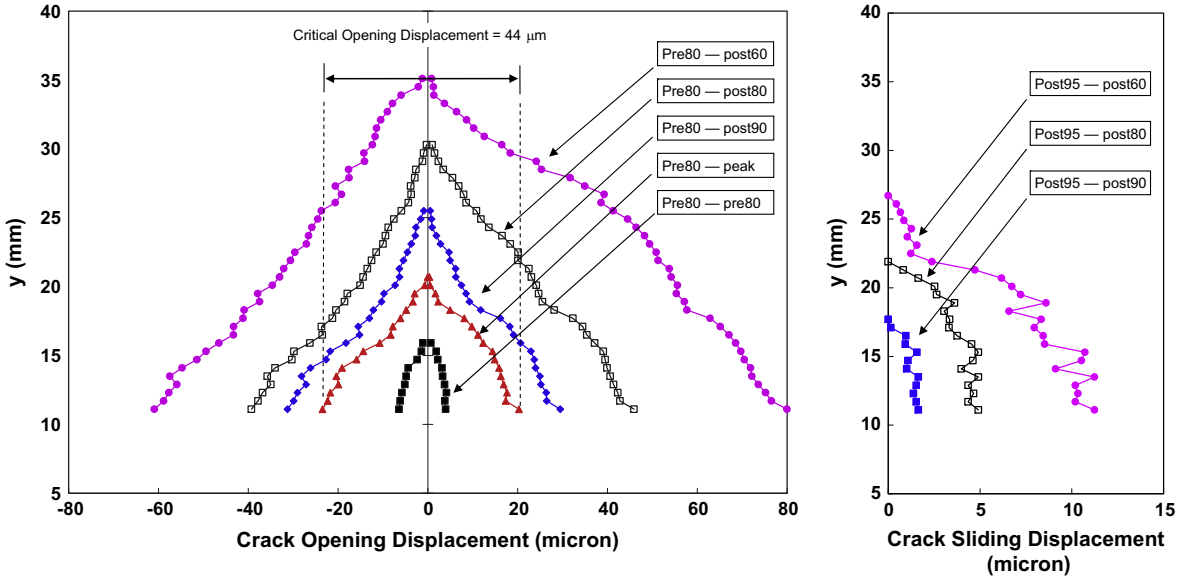

Fig. 10. Total displacements along the fracture, specimen EN-40-20-2. (a) opening displacement; (b) sliding displacement.

that δ in Fig. 10b are the differences between the measured tangential displacements at two sides along the y_1-axis. It is interesting to observe that the total sliding displacement at the notch tip was about 11 μm when the load reached 60% of post-peak, less than 10% of the opening displacement, 140 μm.

Similar to the mode I experiments, the critical crack opening displacement was measured at peak load and used to determine the characteristics of the cohesive zone, along with the crack opening displacement profile at various stages of loading. For example, the position y = 16 mm is where ω_c = 44 μm marks the end of the cohesive zone at loading of 90% post-peak; of course, this is the average value from the left and right sides of the profile, since it is reasonable that the measured displacements are not symmetric (Fig. 10a). Interestingly, this position approximately coincides to the beginning of the slip zone, y = 17 mm, that was determined from crack sliding displacements in Fig. 10b at loading of 90% post-peak. Similar observations were obtained for other loadings (Fig. 10b) and other specimens too. It implies that the opening zone between the tip of CZ and beginning of SZ in Figs. 8 and 9 is the cohesive zone, and SZ is the traction-free portion of the crack. Thus, the cohesive

zone in mixed mode fracture with $K_{II}/K_I < 12\%$ is associated with opening displacement only, and it remained more or less constant, 10–12 mm, as the crack propagated.

5. Conclusions

The full-field displacements measured by digital image correlation (DIC) supply detailed information to study the fracture processes under opening and mixed mode loading. The results from a series of experiments with sandstone specimens containing center and eccentric notches at various positions were presented. The normal/opening and tangential/sliding displacement contours clearly indicated that fracture initiation and propagation were related to the formation of a cohesive zone dominated by opening displacement, in spite of the loading conditions. The measured displacement contours provided evidence that mixed mode loading still leads to opening mode fracture for $K_{II}/K_I < 12\%$.

The maximum crack opening displacement at the notch tip when peak load was reached was assumed to be the critical value for defining the cohesive zone, and these values were about 30 μm for mode I fracture and 45 μm for mixed mode fracture ($K_{II}/K_I < 12\%$.). The tip of the cohesive zone was identified by the merging of the displacement contours. The length of the cohesive zone at peak load was observed to be more or less constant for the quasi-brittle material, but it varied with the fracture mode. For opening, the length was 5–7 mm, about ten times the largest grain size of the sandstone. For mixed mode fracture, the zone length at peak load increased to 10–12 mm. The length of the zone did not change with crack growth for opening and mixed mode fracture.

Acknowledgement

The authors sincerely thank the financial support from NSF grant CMMI-0825454, the MSES/Miles Kersten Chair, the National Natural Science Foundation of China (Grant No. 51304225), and the Science Foundation of China University of Petroleum, Beijing (No. 2462013YJRC036).

References

[1] Whittaker BN, Singh RN, Sun G. Rock fracture mechanics principle design and applications. London: Elsevier; 1992.
[2] van Mier JGM. Fracture process of concrete. Florida: CRC Press; 1997.
[3] Erdogan F, Sih GC. On the crack extension in plates under plane loading on transverse shear. J Basic Eng 1963;85:519–23.
[4] Cotterell B, Rice JR. Slightly curved or kinked cracks. Int J Fract 1980;16(2):155–69.
[5] Bažant ZP, Pfeiffer PA. Shear fracture tests of concrete. Mater Struct 1986;19:111–21.
[6] Ingraffea AR, Panthaki MJ. Analysis of shear fracture tests of concrete beams. In: Meyer, Okamura, editors. Finite Element Analysis of Reinforced Concrete Structures. New York: American Society of Civil Engineers; 1986. p. 151–73.
[7] Rots JG, de Borst R. Analysis of mixed-mode fracture in concrete. J Eng Mech ASCE 1987;113(11):1739–58.
[8] Carpinteri A, Valente S, Ferrara G, Melchiorri G. Is mode II fracture energy a real material property? Comput Struct 1993;48(3):397–413.
[9] Rao Q, Sun Z, Stephansson O, Li C, Stillborg B. Shear fracture (mode II) of brittle rock. Int J Rock Mech Min Sci 2003;40:355–75.
[10] Labuz JF, Riedel JJ, Dai ST. Shear fracture in sandstone under plane-strain compression. Eng Fract Mech 2006;73:820–8.
[11] Backers T, Stephansson O. ISRM suggested method for the determination of mode II fracture toughness. Rock Mech Rock Eng 2012;45(6):1011–22.
[12] Gálvez JC, Cendón DA, Planas J. Influence of shear parameters on mixed-mode fracture of concrete. Int J Fract 2002;118:163–89.
[13] Lin Q, Fakhimi A, Haggerty M, Labuz JF. Initiation of tensile and mixed-mode fracture in sandstone. Int J Rock Mech Min Sci 2009;46:489–97.
[14] Lin Q, Biolzi L, Labuz JF. Opening and mixed-mode fracture initiation in a quasi-brittle material. J Eng Mech ASCE 2013;139:177–87.
[15] Barenblatt GI. The mathematical theory of equilibrium cracks in brittle fracture. Adv Appl Math 1962:56–129.
[16] Labuz JF, Shah SP, Dowding CH. The fracture process zone in granite: evidence and effect. Int J Rock Mech Min Sci Geomech Abstr 1987;24(4):235–46.
[17] Biolzi L. Mixed-mode fracture in concrete beams. Eng Fract Mech 1990;35(1–3):187–93.
[18] Chu TC, Ranson WF, Sutton MA, Peters WH. Applications of digital-image-correlation techniques to experimental mechanics. Exp Mech 1985:232–44.
[19] White DJ, Take WA, Bolton MD. Soil deformation measurement using particle image velocimetry (PIV) and photogrammetry. Geotechnique 2003;53(7):619–31.
[20] Raffel M, Willert CE, Wereley ST, Kompenhans J. Particle image velocimetry. New York: Springer; 2007.
[21] Sutton MA, Orteu J, Schreier HW. Image correlation for shape motion and deformation measurements. New York: Springer; 2009.
[22] Roux S, Réthoré J, Hild F. Digital image correlation and fracture: an advanced technique for estimating stress intensity factors of 2D and 3D cracks. J Phys D Appl Phys 2009;42:214004. Doi: 10.1088/0022-3727/42/21/214004.
[23] Pan B, Qian K, Xie H, Asundi A. Two-dimensional digital image correlation for in-plane displacement and strain measurement: a review. Meas Sci Technol 2009;20:062001. Doi: 10.1088/0957-0233/20/6/062001.
[24] Nguyen TL, Hall SA, Vacher P, Viggiani G. Fracture mechanism in soft rock: identification and quantification of evolving displacement discontinuities by extended digital image correlation. Tectonophysics 2011;503:117–28.
[25] Shen B, Paulino GH. Identification of cohesive zone model and elastic parameters of fiber-reinforced cementitious composites using digital image correlation and a hybrid inverse technique. Cement Concr Compos 2011;33:572–85.
[26] Leplay P, Réthoré J, Meille S, Baietto MC. Identification of damage and cracking behaviours based on energy dissipation mode analysis in a quasi-brittle materials using digital image correlation. Int J Fract 2011;171:35–50.
[27] Lin Q, Labuz JF. Fracture of sandstone characterized by digital image correlation. Int J Rock Mech Min Sci 2013;60:235–45.
[28] Yamaguchi I. Speckle displacement and decorrelation in the diffraction and image fields for small object deformation. Opt Acta 1981;28:1359–76.
[29] Peters WH, Ranson WF. Digital imaging techniques in experimental stress analysis. Opt Eng 1982;21(3):427–31.
[30] Bruck HA, McNeill SR, Sutton MA, Peters WH. Digital image correlation using a Newton–Raphson method of partial differential correlation. Exp Mech 1989:261–7.
[31] Pan B, Asundi A, Xie H, Gao J. Digital image correlation using iterative least squares and pointwise least squares for displacement field and strain field measurements. Opt Laser Eng 2009;47:865–74.
[32] White DJ, Take WA. GeoPIV: Particle Image Velocimetry (PIV) software for use in geotechnical testing. CUED/D-SOILS/TR322; 2002.
[33] Chen DJ, Chiang FP, Tan YS, Don HS. Digital speckle-displacement measurement using a complex spectrum method. Appl Opt 1993;32(11):1839–49.
[34] Liu J, Iskander M. Adaptive cross correlation for imaging displacements in soils. J Comput Civil Eng 2004;18:46–57.

[35] Ostanin IA, Mogilevskaya SG, Labuz JF, Napier J. Complex variables BEM for elasticity problems with constant body force. Eng Anal Bound Elem 2011;35:623–30.
[36] Haggerty M, Lin Q, Labuz JF. Observing deformation and fracture of rock with speckle pattern. Rock Mech Rock Eng 2010;43:417–26.
[37] Zietlow WK, Labuz JF. Measurement of the intrinsic process zone in rock using acoustic emission. Int J Rock Mech Min Sci 1998;35:291–9.
[38] Otsuka K, Date H. Fracture process zone in concrete tension specimen. Eng Fract Mech 2000;65:111–31.